

## Article

# Precipitation Behavior and Microstructural Evolution of $\alpha$ Phase during Hot Deformation in a Novel $\beta$ -Air-Cooled Metastable $\beta$ -Type Ti-B12 Alloy

Jun Cheng <sup>1,\*</sup>, Sen Yu <sup>1</sup>, Jinshan Li <sup>2</sup>, Jinyang Gai <sup>3</sup>, Zhaoxin Du <sup>4</sup>, Fuyu Dong <sup>5</sup>, Jinyong Zhang <sup>6</sup> and Xiaoyong Zhang <sup>3</sup>

- <sup>1</sup> Shaanxi Key Laboratory of Biomedical Metal Materials, Northwest Institute for Nonferrous Metal Research, Xi'an 710016, China; yusen\_1982@126.com
- <sup>2</sup> State Key Laboratory of Solidification Processing, Northwestern Polytechnical University, Xi'an 710072, China; ljsh@nwpu.edu.cn
- <sup>3</sup> State Key Laboratory of Powder Metallurgy, Central South University, Changsha 410083, China; 203301071@csu.edu.cn (J.G.); zhangxiaoyong@csu.edu.cn (X.Z.)
- <sup>4</sup> School of Materials Science and Engineering, Inner Mongolia University of Technology, Hohhot 010051, China; duzhaoxin@163.com
- <sup>5</sup> School of Materials Science and Engineering, Shenyang University of Technology, Shenyang 110870, China; dongfuyu2002@163.com
- <sup>6</sup> School of Material Science and Engineering, China University of Mining and Technology, Xuzhou 221008, China; jy Zhang@cumt.edu.cn
- \* Correspondence: chengjun\_851118@126.com



**Citation:** Cheng, J.; Yu, S.; Li, J.; Gai, J.; Du, Z.; Dong, F.; Zhang, J.; Zhang, X. Precipitation Behavior and Microstructural Evolution of  $\alpha$  Phase during Hot Deformation in a Novel  $\beta$ -Air-Cooled Metastable  $\beta$ -Type Ti-B12 Alloy. *Metals* **2022**, *12*, 770. <https://doi.org/10.3390/met12050770>

Academic Editor: Ling Ren

Received: 26 March 2022

Accepted: 21 April 2022

Published: 29 April 2022

**Publisher's Note:** MDPI stays neutral with regard to jurisdictional claims in published maps and institutional affiliations.

**Abstract:** The precipitation behavior and microstructural evolution of  $\alpha$  phase in a novel metastable  $\beta$ -type Ti alloy, Ti-10Mo-6Zr-4Sn-3Nb (wt.%), during isothermal compression are investigated in this study through the use of SEM (scanning electron microscope), TEM (transmission electron microscope) (HRTEM) (high-resolution transmission electron microscopy) and EBSD techniques. The results show that some finer  $\alpha$  precipitates are randomly distributed within the  $\beta$  matrix during hot deformation. The morphological characteristics of  $\alpha$  precipitates are distinctly different from those of  $\alpha$  precipitates during the same solution-plus-aging treatment. The volume fraction of  $\alpha$  precipitate gradually increases with increased true strain. A large proportion of precipitated  $\alpha$  phases are prone to be precipitated at HAGBs (high-angle grain boundaries) and LAGBs (low-angle grain boundaries) during isothermal deformation. On the contrary, only a small amount of spherical  $\alpha$  phases is precipitated within the  $\beta$  grain. The crystallographic orientation relationships for most spherical  $\alpha$  precipitates formed at LAGBs and within the  $\beta$  grains are similar, whereas the crystallographic orientation relationships for  $\alpha$  precipitates at grain boundaries are significantly different. The precipitation behavior of  $\alpha$  phase in the Ti-B12 alloy during hot compression is considerably influenced by the density of dislocations.

**Keywords:** metastable  $\beta$ -type Ti alloy; isothermal compression; precipitation behavior; variant selection; thermal-mechanical asymmetric coupling



**Copyright:** © 2022 by the authors. Licensee MDPI, Basel, Switzerland. This article is an open access article distributed under the terms and conditions of the Creative Commons Attribution (CC BY) license (<https://creativecommons.org/licenses/by/4.0/>).

## 1. Introduction

Metastable  $\beta$ -type Ti alloy is regarded as an extremely promising functional rare metal in strategic industries including aerospace, ballistic protection, marine engineering and biomedical applications due to its high strength, outstanding fatigue properties, excellent cold/hot processing properties, low Young's modulus and prominent work-hardening effect [1–3]. For example, Ti-3.5Al-10Mo-8V-1Fe (TB3), Ti-15333 (TB5), Ti-1023 (TB6),  $\beta$ -21S (TB8) and Ti-55531 alloy products have been successfully applied in large-size forgings of civil aircraft, such as in the Boeing 777 and Boeing 787 of USA, as well as China's C919 [4,5]. It is worth mentioning that TB3 bars are successfully used to manufacture fasteners in

aircraft [6]. The room-temperature mechanical performances of metastable  $\beta$ -type Ti alloy are significantly influenced by microstructural features, including the volume fraction, size, morphological characteristics and distribution pattern of precipitated  $\alpha$  phase within the  $\beta$  matrix [7–10]. Compared with the  $(\alpha + \beta)$ -type Ti alloy, the above parameters for  $\beta$ -type Ti alloy are extremely sensitive to the factors including heating temperature, holding time, cooling method and heating rate during the thermomechanical treatment [11,12]. For instance, the equiaxed and lath-like precipitated  $\alpha$  phase in Ti alloy presents a significant difference in room-temperature strength, plasticity, microhardness and fatigue limit [13,14].

A large amount of research has been performed in recent years, focusing on the microstructural evolution of precipitated  $\alpha$  phase in the  $(\alpha + \beta)$ - and metastable  $\beta$ -type Ti alloys, such as Ti-6Al-4V, Ti-1023, Ti-5553 and Ti-55511 alloy, which are subjected to conventional heat treatment or hot working [15–18]. These studies can help to better understand the necessity of precise control of the microstructure and further optimization of mechanical performances. Most of investigations on the precipitation behavior and evolutionary mechanisms of precipitated  $\alpha$  phase have been focused on the process control of heat treatment. Qian et al. discussed the phase decomposition and precipitation behavior of  $\alpha$  precipitate in Ti-6Cr and Ti-11Mo binary alloys after  $\beta$ -solution treatment followed by water quenching plus aging [19]. It was found that the discontinuous growth of the secondary phase appeared in the transformed region, which was composed of several parallel laths. These laths gradually grew from the areas of  $\beta$  grain boundary into the inside of the  $\beta$  matrix [20,21]. However,  $\alpha$  phases in the alloys subjected to aging were continuously precipitated in the whole region, and the driving force for precipitation was significantly improved [22,23]. Dye et al. studied the effect of nucleation and precipitation behavior for the secondary phase in Ti-5553 alloy through the use of various heat-treatment routes [24]. Moreover, the precipitation and growth rate of  $\alpha$  phase was relatively slower during aging in Ti-5553 alloy. In the process of solution-plus-aging treatment, some precipitated  $\alpha$  phases with various morphological characteristics were also examined in typical metastable  $\beta$ -type Ti alloys, for instance, TB5 and Ti-4.5Fe-6.8Mo-1.5Al alloys [25,26]. In addition, the study on the precipitation behavior of  $\alpha$  phases in the process of isothermal compression deformation was primarily focused on the Ti-6Al-4V alloy. Zharebtsov et al. have discussed the whole process of spheroidization evolution of lath-like  $\alpha$  precipitates in Ti64 alloy during thermomechanical treatments [27]. The lath structure was gradually transformed into a spherical structure by the formation of dislocation walls and a grain-boundary separation mechanism. With the decrease in temperature, the possibility of shearing deformation could increase. On the contrary, the volume fraction of the parent  $\beta$  matrix could decrease correspondingly, resulting in inhomogeneous deformation. Compared with  $(\alpha + \beta)$  Ti alloys, the nucleation and growth of precipitated  $\alpha$  phases are extremely sensitive to the molybdenum equivalent ( $[Mo]_{eq}$ ) and mutual diffusion of alloying elements between different phases in some metastable  $\beta$ -Ti alloys [28]. It is noted that the molybdenum equivalent is often considered one of the critically significant factors for the design of novel biomedical Ti alloys. The precipitation behavior and microstructural evolution of precipitated  $\alpha$  phase are also greatly influenced by the molybdenum equivalent. They mainly depend on the type of newly added alloying elements, such as Zr, Mo, Sn, Al, Cr, Nb and V. Owing to the modification of various alloying elements, the influences of interdiffusion of alloying elements are completely distinct in influencing the nucleation and precipitation behavior of  $\alpha$  phase [29]. Until now, few reports have focused on the nucleation and growth behavior of precipitated  $\alpha$  phase in metastable  $\beta$ -type Ti alloys during hot compression. Therefore, more theoretical analyses and experimental research still need to be conducted in an attempt to clarify precipitation behavior and its corresponding mechanism of  $\alpha$  phase in metastable  $\beta$ -Ti alloys during hot working.

The precipitation behavior and microstructural evolution of precipitated  $\alpha$  phase in a novel biomedical metastable  $\beta$ -type Ti-10Mo-6Zr-4Sn-3Nb (Ti-B12) alloy during hot compression is investigated in this work. Morphological characteristics and crystallographic orientation evolution of  $\alpha$  phase in the Ti-B12 alloy during hot compression are discussed

in detail. The acquired results of this study can provide valuable theoretical guidance for a better understanding of the microstructural evolution and precipitation mechanism of  $\alpha$  phase during hot deformation.

## 2. Experimental Materials and Methods

### 2.1. Ti-B12 Alloy Preparation and Processing

A Ti-B12 alloy ingot of 160 mm diameter was fabricated using vacuum arc remelting four times in order to ensure high consistency of chemical composition and avoid the occurrence of elemental segregation. The ingot was homogenized in an electric furnace (KSL-1200X, 3.5 KW, Kejing Materials Technology Co., Ltd., Hefei, China) at 1150 °C for 10 h. The ingot was multidirectionally forged three times in the  $\beta$ -phase region (1080 °C) to break the initial coarse as-cast microstructures and achieve fairly refined grains. The free forging of square rods and hot continuous rolling of round bars were performed in the ( $\alpha + \beta$ )-phase region (700~740 °C). Finally, the final products with a diameter of 10.5 mm were manufactured after straightening and mechanical polishing. Ti-B12 alloy was originally developed by the Northwest Institute for Nonferrous Metal Research (NIN) (Xi'an, China) as a novel metastable  $\beta$ -type Ti alloy for surgical implants [30–32]. Compared with the  $\alpha$  and ( $\alpha + \beta$ ) Ti alloy, Ti-B12 alloy possesses higher yield strength-to-elastic modulus ratio, excellent workability, good biocompatibility and non-toxicity. The molybdenum equivalent was calculated to be about 10.9 using an empirical equation, which is similar to that of  $\beta$ III alloy (Ti-11.5Mo-6Zr-4.5Sn). It can be seen from Figure 1 that the equiaxed primary  $\alpha$  phases ( $\alpha_p$ ) were dispersedly distributed within the  $\beta$  matrix. The  $\beta$  transus temperature for this alloy determined by the metallographic method and DSC (differential scanning calorimetry) curves was close to 750~755 °C.

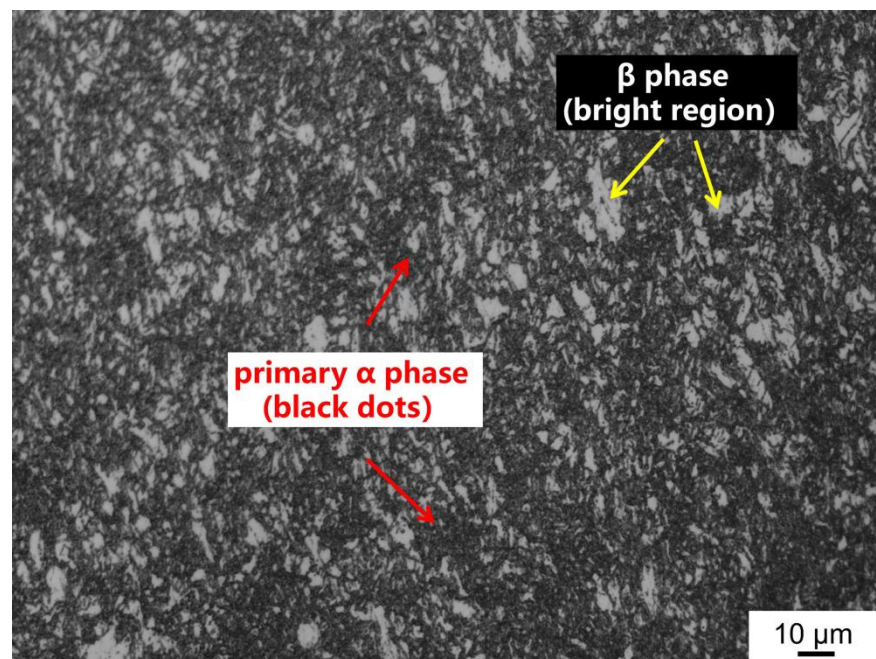


**Figure 1.** Hot-rolled microstructure (1000 $\times$ ) of Ti-B12 alloy.

### 2.2. Isothermal Compression Testing

Isothermal compression testing was performed on a Gleeble-3800 instrument (DSI company, New York, NY, USA). The compressed samples (diameter: 8 mm, height: 12 mm, surface roughness: 0.8  $\mu$ m) were machined using electric discharge machining (EDM) (SHANGHAI ESUNTEK, Shanghai, China) and CNC (computer numerical control) machining (BAOJI MACHINE TOOL GROUP Co., Ltd., Baoji, China). The K-type thermocouple sensors were spot-welded in the middle of the specimen in an attempt to accurately control

and monitor the deformation temperature and strain rate. Two pieces of FTa-1 (purity of more than 99.95%) foils with a thickness of 0.16 mm were placed between the specimen and compression mold to reduce friction and avoid the appearance of flow instability, such as shearing deformation and cracking. First, the samples were solution-treated in the  $\beta$  single-phase region (790 °C) for 1 h using an electrical-resistance furnace before hot compression. Air cooling was carried out immediately once the holding time was over. The microstructural morphology of Ti-B12 alloy subjected to  $\beta$ -solution treatment is shown in Figure 2. The solution-treated sample is composed of equiaxed  $\beta$  grains. The average grain size was calculated by Image J analysis software to be 68  $\mu\text{m}$ . Meanwhile, there were some flow lines in the  $\beta$  matrix due to previous hot rolling of the bar. The results of XRD (X-ray Diffraction) (Bruker, Karlsruhe, Germany) analysis of the profile revealed that there was no trace of  $\alpha$  precipitate in the Ti-B12 alloy subjected to  $\beta$ -solution treatment followed by air cooling. Isothermal compression testing was conducted at a deformation temperature of 550 °C and a strain rate of  $0.001 \text{ s}^{-1}$ . The heating rate was set to 30 °C/s, and the holding time was determined to be 30 s. When the experiment was completed, the compressed specimens were immediately taken out of the vacuum chamber of the Gleeble-3800 tester (DSI company, New York, NY, USA) and water-quenched to retain the deformed microstructure at room temperature. The time it took to complete the whole process was about 2–3 s. All of the hot-compression experiments were performed under the high-vacuum condition (vacuum degree:  $5 \times 10^{-3} \text{ Pa}$ ). The true strain values were determined to be 0.6, 0.8 and 1.2, respectively, in an attempt to investigate the influence of deformation reduction on microstructural evolution during isothermal compression. The experimental procedure is shown in Figure 3. The serrated part represents isothermal compression deformation rather than temperature fluctuation. In this process, the deformation temperature was constant.

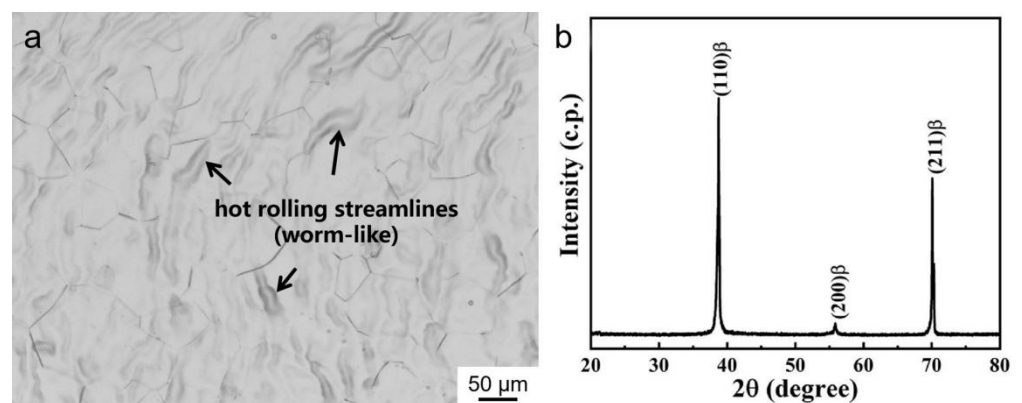


**Figure 2.** The  $\beta$ -solution-treated microstructure (a) and XRD pattern (b) of Ti-B12 alloy before isothermal deformation test.

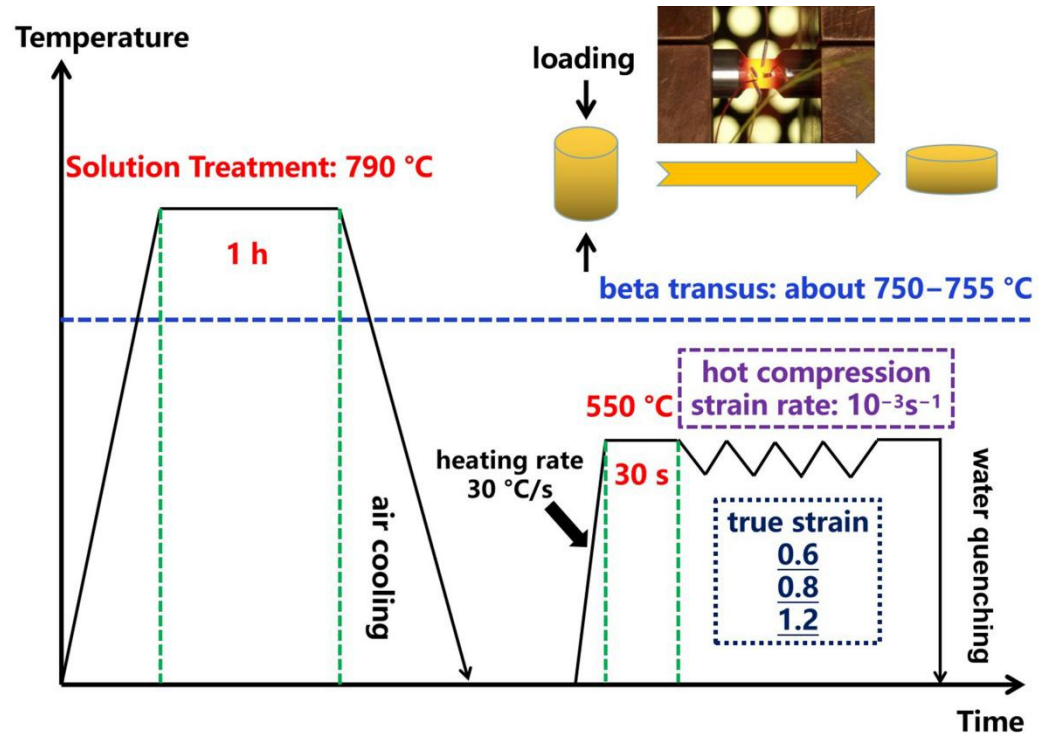


Figure 3. A schematic diagram of the isothermal deformation test.

The severe compressive deformation zone in the center of the specimen was selected as the observed region in this work. The metallographic sections were sampled from similar positions in each specimen. The true strain/temperature history at these locations were subject to unknown variability and error between specimens. The alloy sample was etched using Kroll's solution (15% HF: 15%, HNO<sub>3</sub>: 70%, H<sub>2</sub>O, vol.%) to show the morphology of deformed microstructure under various conditions. The surface of the specimen required for EBSD characterization should be smooth without residual stress, in an attempt to achieve high-resolution images. The sample was prepared by electrolytic polishing using a Buehler ElectroMet 4 instrument. The solution for electrolytic polishing was composed of 8% perchloric acid and 92% ethanol, with a voltage of 37 V for 240 s at 28 °C. The prepared specimen was analyzed using an FEI Quanta FEG 250 field emission scanning electron microscope (FESEM) (FEI, Hillsboro, OR, USA) equipped with an Oxford Instruments EBSD detector (Oxford Instruments, Oxford, UK). EBSD measurement was performed at an accelerating voltage of 22 kV, and the data were further processed using HKL Channel 5 software (Oxford Instruments Company, Abingdon, UK). The random distribution of crystallographic orientation and higher image noise could be caused by the effect of severe plastic deformation in the center of the specimen, resulting in an obvious decrease in the resolution rate of EBSD maps. Therefore, grain boundaries and phase interfaces became indistinguishable, and misorientation angles of less than 2° were difficult to be completely marked by Channel 5 software. In general, the misorientation angles located in the range of 2–15° were defined as low-angle grain boundaries (LAGBs). Moreover, we defined misorientation angles >15° as high-angle grain boundaries (HAGBs). The quantitative characterization of the hot-compressed microstructure was conducted with the help of Photoshop CS6 (64 bit) (Adobe Systems, Mountain View, CA, USA) and Image-Pro Plus commercial software (Media Cybernetics, Inc., Rockville, MD, USA). TEM foils with a thickness of 0.6 mm were cut from alloy bars by an EDM machine. Subsequently, they were mechanically thinned to approximately 40 μm in thickness using SiC waterproof papers (200–5000#). The observed area was prepared using ion beam thinning on a Gatan-691 instrument. Finally, morphological observation and microstructural analysis were

conducted on an FEI G2 F30 TEM (FEI, Eindhoven, The Netherlands) operating at an accelerating voltage of 200–300 kV.

### 3. Results and Discussion

#### 3.1. Hot-Deformed Microstructural Characteristics under Various True Strains

The SEM images of the microstructural morphology of Ti-B12 alloy subjected to hot compression at various true strains are presented in Figure 4. It can be clearly seen from the above figures that a small amount of  $\alpha$  precipitates is formed within the  $\beta$  matrix. The density of precipitated  $\alpha$  phases gradually increases with an increase in the true strain during isothermal compression. According to the statistics, the volume fraction of the alpha phase is increased from approximately 15% to 80%. In addition, the morphology of precipitated  $\alpha$  phases near the  $\beta$  grain boundary is a finer lath shape, and the non-uniform distribution of  $\alpha$  precipitates can be observed within the  $\beta$  grains. In general, the precipitated  $\alpha$  phases are evidenced by either lath-like or needle-like features at the grain boundaries and within the  $\beta$  matrix during conventional heat treatments. Nevertheless, a large amount of small, spherical precipitated  $\alpha$  phases are mainly formed in the  $\beta$  grains of Ti-B12 alloy after isothermal compression. Based on the literature [33,34], it can be concluded that the size of  $\alpha$  precipitates within grains or on the grain boundaries after isothermal deformation is apparently finer than that of  $\alpha$  precipitates under the same heat-treatment condition. The nucleation and growth of  $\alpha$  precipitates are primarily regulated by the diffusion and redistribution of alloying elements during solution-plus-aging treatment. The diverse morphological characteristics of precipitated  $\alpha$  phase indicate that the secondary phase is simultaneously influenced by the mutual diffusion of alloying elements and dynamic loading during hot deformation, namely a thermal-mechanical asymmetric coupling role. The lamellar  $\alpha$  phases are gradually transformed into spherically shaped precipitates near the grain boundaries under compression loading, resulting in increased workability and a refined microstructure [35].

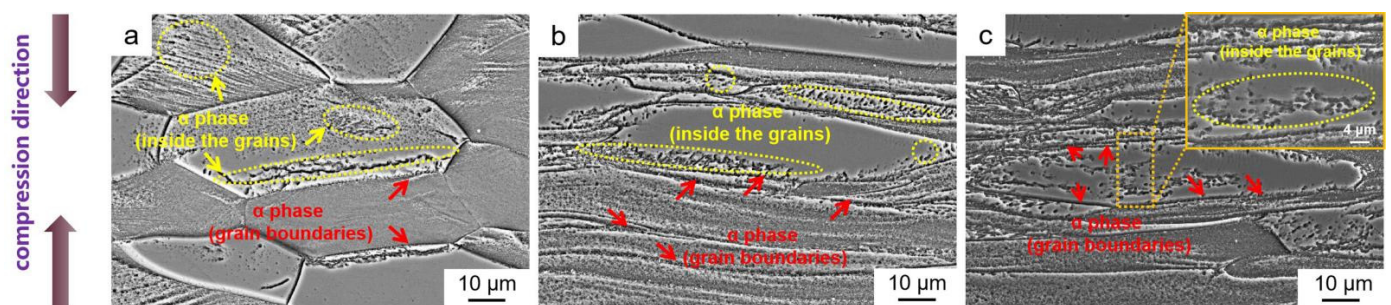


**Figure 4.** The hot-compressed microstructure of Ti-B12 alloy at different true strains: (a) 0.6, (b) 0.8 and (c) 1.2.

Electron backscattering diffraction (EBSD) is used to quantitatively characterize the microstructural morphology, preferred orientation, grain boundary types and crystal orientation in metallic materials. As shown in Figure 5, EBSD maps are composed of the inverse pole figure (IPF) map and grain boundary distribution mapping (such as LAGBs and HAGBs). The IPF figure of  $\beta$  matrix and  $\alpha$  phase is presented in Figure 5a. LAGBs (gray) and HAGBs (black) are distinguished with various colors, as shown in Figure 5b. The  $\beta$  grains are obviously elongated and flattened perpendicularly to the loading direction after hot compression at 550 °C. At the same time, the continuous grain boundaries are split into several discontinuous parts. The boundaries of flattened  $\beta$  grains are relatively straight, and there are a few fine recrystallized grains with necklace shape in the vicinity of grain boundaries. The phenomenon of dynamic recrystallization is caused in some  $\beta$  grains under the isothermal compression condition, promoting grain refinement and improvement of mechanical properties in the Ti-B12 alloy.

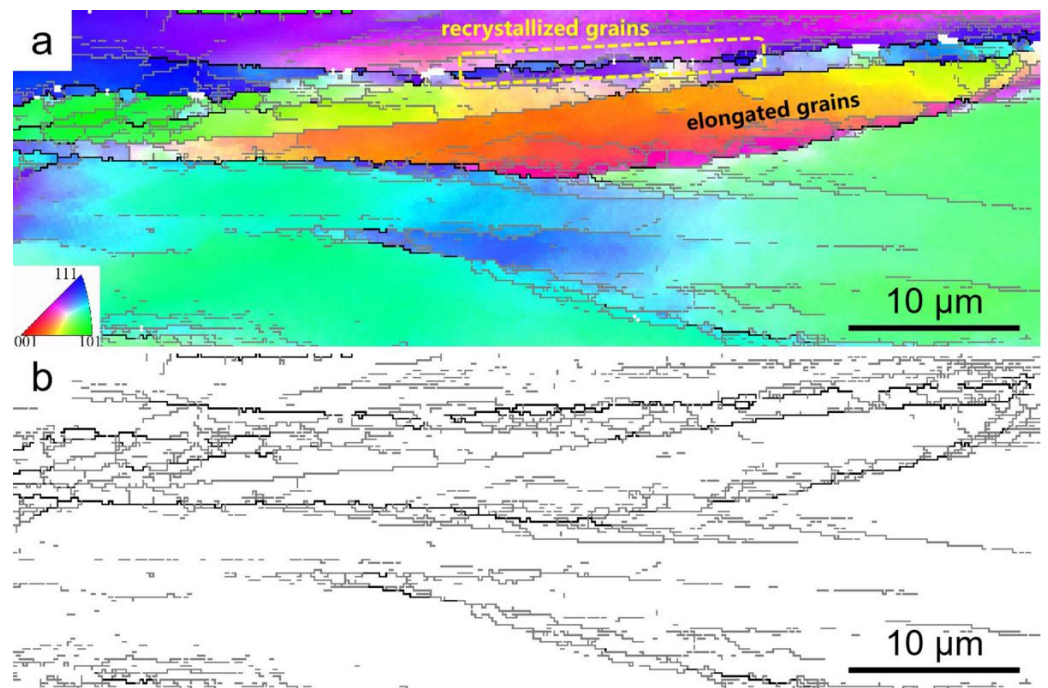


**Figure 5.** EBSD images of hot-compressed microstructures of Ti-B12 alloy at a true strain of 0.8: (a) IPF figure; (b) grain boundary distribution mapping.

### 3.2. Precipitation Behavior of $\alpha$ Phase

A large proportion of the  $\alpha$  precipitates is prone to be formed at HAGBs and LAGBs. There is also a small amount of spherical  $\alpha$  precipitates appearing within the elongated grains. The  $\alpha$  phases precipitated at the  $\beta$  grain boundaries have peculiar crystallographic variants, owing to their different crystallographic orientation relationship between two phases. The formation of secondary phases and hot-compressed morphological features for Ti-B12 alloy can be analyzed in depth using the TEM technique, as shown in Figure 6. It can be observed from Figure 6a that there are many dislocation line segments and dislocation cell walls in the  $\beta$  grains after hot compression at under certain strain. In the process of hot compression, a large amount of dislocations begins to gradually move and slip within the  $\beta$  grains, resulting in dislocation tangles and the formation of dislocation walls [36]. It is interesting to note that some dislocations eventually evolve into a sawtooth-shape (Figure 6b). In addition, cross-linking between dislocations was induced in the form of dislocation tangles, resulting in an increase in dislocation density in the local region after hot compression.

As shown in Figure 7, hot compression can give rise to the precipitation of grain boundary  $\alpha$  phase with a size of about 2.5  $\mu\text{m}$  in length and 600 nm in width. Some needle-like  $\alpha$  precipitates are also discontinuously distributed in the  $\beta$  matrix. It can be seen from Figure 7b that the angle between two adjacent precipitated  $\alpha$  phases is approximately  $15^\circ$ . Moreover, some  $\alpha$  precipitates that are nearly parallel to each other form on both sides of the  $\beta$  grain boundaries (Figure 7a). The morphology of precipitated  $\alpha$  phases at grain boundaries during hot compression is similar to that of  $\alpha$  precipitates during conventional solution-plus-aging treatment. Nevertheless, the density of dislocations introduced into  $\alpha_{GB}$  phases increases with increased true strain under the combined effects of thermal-mechanical asymmetric coupling, resulting in the formation of dislocation walls and spheroidization of grain boundary  $\alpha$  phase.

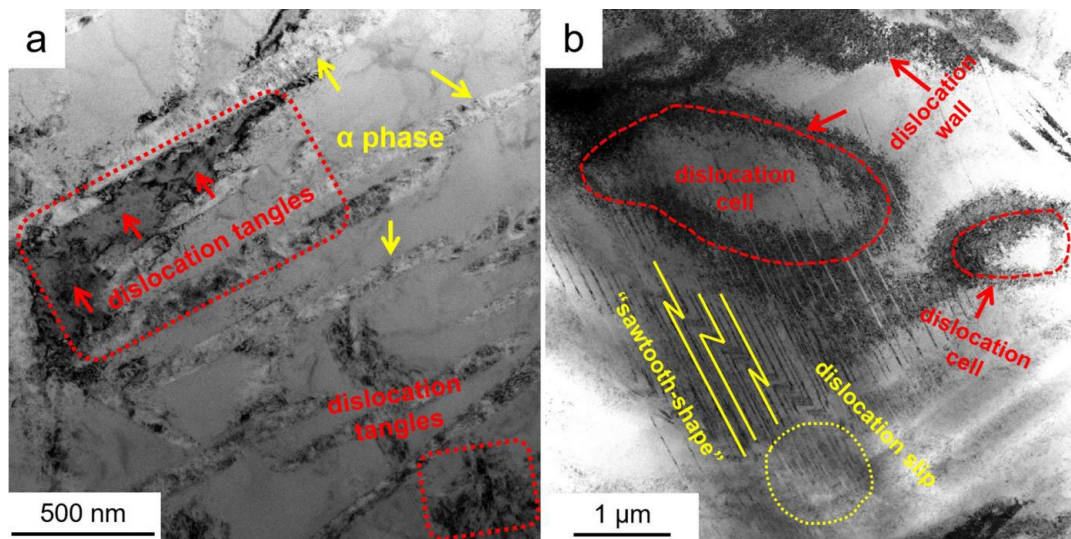


**Figure 6.** TEM images of dislocations in the air-cooled specimen of Ti-B12 alloy after isothermal compression: (a) dislocation tangles; (b) dislocation slip and dislocation cell.

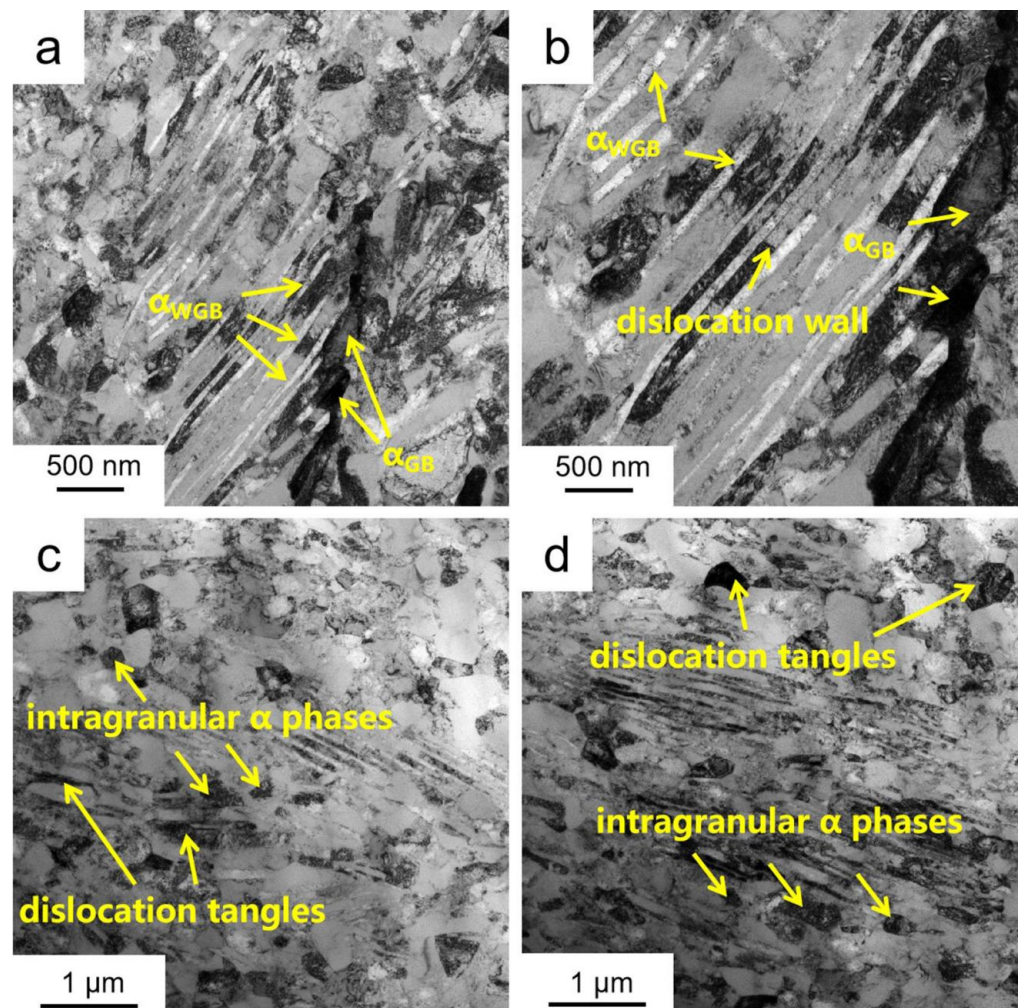


**Figure 7.** Bright-field (BF) TEM images of  $\alpha$  precipitates formed in an air-cooled Ti-B12 alloy after hot compression at a true strain of 0.8: (a,b) grain boundary  $\alpha$  phases; (c,d)  $\alpha$  precipitates inside of  $\beta$  grains.

In general, dislocation is a type of line defect that is often considered the nucleation site of the secondary phase at the grain boundary during deformation. The variant selection of  $\alpha_{GB}$  phase and subsequent texture evolution during phase transition are sensitively affected by dislocation. The density of dislocation in the severe deformation region significantly increases with an increase in true strain, leading to local stress concentration in certain areas. In response, more preferred slip systems are activated in order to effectively alleviate the degree of stress concentration during deformation. The discontinuous  $\alpha_{GB}$  dislocation tangles and dislocation glide/climb are promoted by the synergistic interactions between deformation bands and grain boundaries.

Furthermore, it can be seen from Figure 5a that the crystallographic orientations of precipitated  $\alpha$  phase in the parent  $\beta$  phase are basically the same. A small number of refined spherical  $\alpha$  precipitates are formed within the  $\beta$  grains after hot compression. The size of intragranular  $\alpha$  phase is approximately 0.6  $\mu\text{m}$ , as shown in Figure 7c. It is also observed that the morphological characteristics and crystallographic orientations of hot-compressed alloy are completely different from those of the Ti-B12 alloy subjected to traditional solution-plus-aging treatment. The precipitated  $\alpha$  phase has an HCP crystallographic structure and the number of predominant slip systems is also limited, resulting in an increase in the difficulty of plastic deformation [37]. Therefore, it is difficult to completely release the distortions and residual stresses induced by isothermal compression merely depending on the dislocation intercross, pileup and recombination of dislocations. As shown in the bright-field TEM image (Figure 7d), it is difficult to distinguish the  $\alpha/\beta$  interface in the Ti-B12 alloy after hot compression. One main reason is due to relatively higher local stress concentration near the interphase interface, resulting in the appearance of stress gradient distribution from the grain boundary to the grain interior. It can be inferred that most continuous lattice fringes for the interfaces of  $\alpha$  precipitate are partly broken by discontinuous lattices due to the movement of dislocation. Finally, the slipping of partial dislocations results in a blurring effect on the phase interface.

### 3.3. Precipitation Behavior of $\alpha$ Phase and its Formation Mechanism

According to the analysis of the above results, the rapid nucleation and growth of  $\alpha$  precipitates can occur both within  $\beta$  grains and near  $\beta$  grain boundaries during isothermal compression. The grain boundary is composed of a layer of precipitated  $\alpha$  phase. There are also some lath-like  $\alpha$  phases, which are parallel to each other around the grain boundary, and the epitaxial growth direction gradually grows towards the  $\beta$  grain interior. In general, the lath-shaped Widmanstätten  $\alpha$  phase ( $\alpha_W$ ) generated during solution-plus-aging treatment is mainly due to the mutual diffusion of alloying elements and the destabilizing effect of nucleation at the  $\alpha/\beta$  interface [38].

Figure 8 shows a schematic diagram of the precipitation mechanism for  $\alpha$  phase in the Ti-B12 alloy during isothermal compression. The precipitated  $\alpha$  phases formed during hot-compression deformation are simultaneously controlled by crystal defects and local stress concentration. In general, hot compression can drastically increase the volume fraction of LAGBs. LAGBs can be considered preferred nucleation sites that effectively promote the precipitation of  $\alpha$  phase with a similar crystallographic orientation relationship [39]. In addition, large amounts of crystal defects, such as dislocation lines and dislocation cells, are prone to be introduced into the grain interior under the condition of applied stress [40]. These defects can contribute to assisted nucleation of secondary  $\alpha$  phase, possibly resulting in the refinement of spherical  $\alpha$  precipitates. A large number of dislocation tangles near the  $\alpha/\beta$  phase interface or inside of the precipitated  $\alpha$  phase also leads to an effect of local stress concentration during isothermal deformation. Subsequently, more shear bands are induced in the  $\alpha$  phase with an increase in true strain, resulting in dislocation multiplication, as well as formation and migration of dislocation walls in the  $\alpha$  phase. The generation of abundant dislocations results in spheroidization and refinement of  $\alpha$  precipitates to some extent. Finally, equiaxed  $\alpha$  phases with different shapes and sizes are formed, and the microstructural transformation from lamellar to spherical shape is completed.

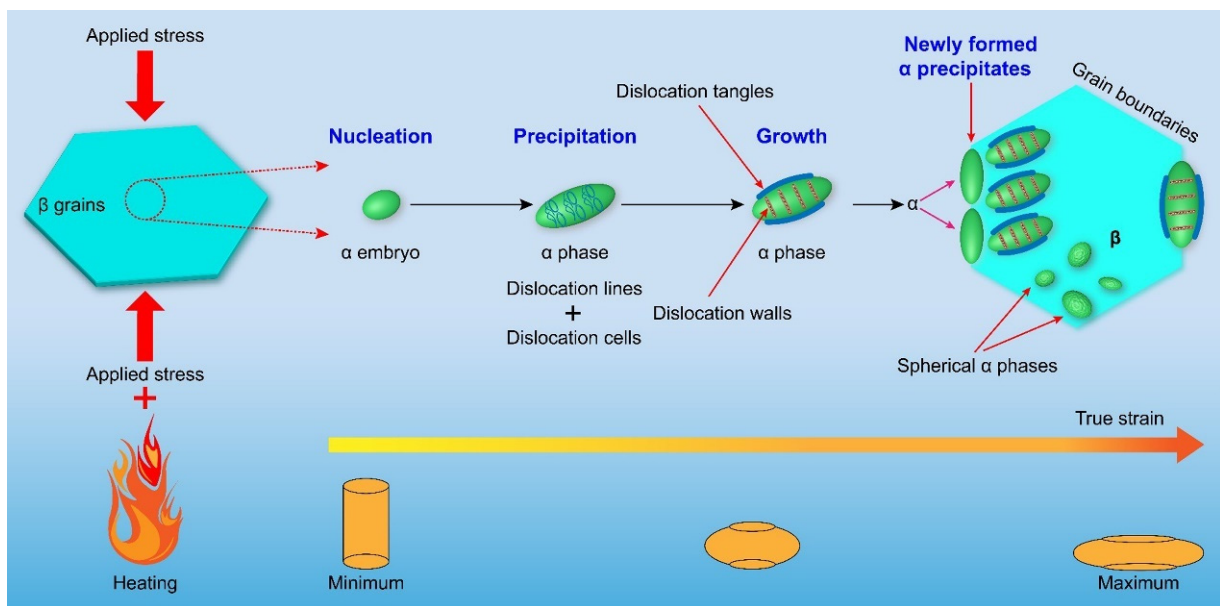


**Figure 8.** Schematic diagram of precipitation behavior for  $\alpha$  phase during isothermal compression.

### 3.4. Crystallographic Orientation Relationship between Precipitated $\alpha$ Phase and Parent $\beta$ Phase

The crystallographic orientation of  $\alpha$  phases (HCP) precipitated at the grain boundaries of the parent  $\beta$  phase (BCC) without plastic deformation has been studied in numerous research works. T. Furuhashi et al. reported that a Burgers orientation relationship exists between precipitated  $\alpha$  phase and at least one of the neighboring  $\beta$  grains in some  $\beta$ -type Ti alloys [41].

In an attempt to determine the crystallographic orientation relationship between precipitated  $\alpha$  phase and parent  $\beta$  phase during hot compression, the pole figures (PFs) of a given local zone obtained from EBSD imaging are illustrated in Figure 9. It can be clearly noted that there is no particular Burgers orientation relationship between precipitated  $\alpha$  phase and parent  $\beta$  phase in the strict sense. The primary reason is that the original orientation relationship between  $\alpha$  precipitate and  $\beta$  changed to some extent after hot compression. Nevertheless, the PFs of  $\alpha_{GB}$  precipitates indicate that a near-Burgers orientation relationship (BOR) is still present between  $\alpha_{GB}$  precipitates and the  $\beta$  matrix. The BOR of spherically shaped precipitated  $\alpha$  phase was destroyed, owing to the effect of spheroidization of the lamellar structure. Therefore, the trend of globularization gradually becomes more obvious with increased true strain during hot compression, and finally, some finer globular  $\alpha$  precipitates are formed within the  $\beta$  matrix. In general, the globularization of lath-like  $\alpha$  phase can be divided into four representative stages: (1) shear loading of the lath-like structure; (2) formation of dislocation structures; (3) thickening of dislocation walls; and (4) dislocation interface separation and disconnection-assisted migration [42,43]. Thus, it is beneficial to further clarify the microstructural evolution mechanisms and distribution characteristics of  $\alpha$  phase in the Ti-B12 alloy during hot compression.

The interface and crystallographic orientation relationship between  $\alpha$  precipitates and the  $\beta$  matrix were further characterized using the HRTEM technique. The  $\alpha/\beta$  crystallographic orientation relationship is as follows:  $[1]\alpha//[110]\beta$  and  $(10-10)\alpha//(-110)\beta$ , as presented in Figure 10. There exists a remarkable variant selection effect on the precipitated  $\alpha$  phase formed at the grain boundaries on the basis of diverse types of grain boundaries and applied loading. The  $\alpha$  precipitates are prone to be generated at LAGBs based on the crystallographic orientation relationship between the precipitated  $\alpha$  phase and the parent  $\beta$  phase. The reason is that the initial continuous grain boundaries were broken by compressive stress during isothermal deformation.

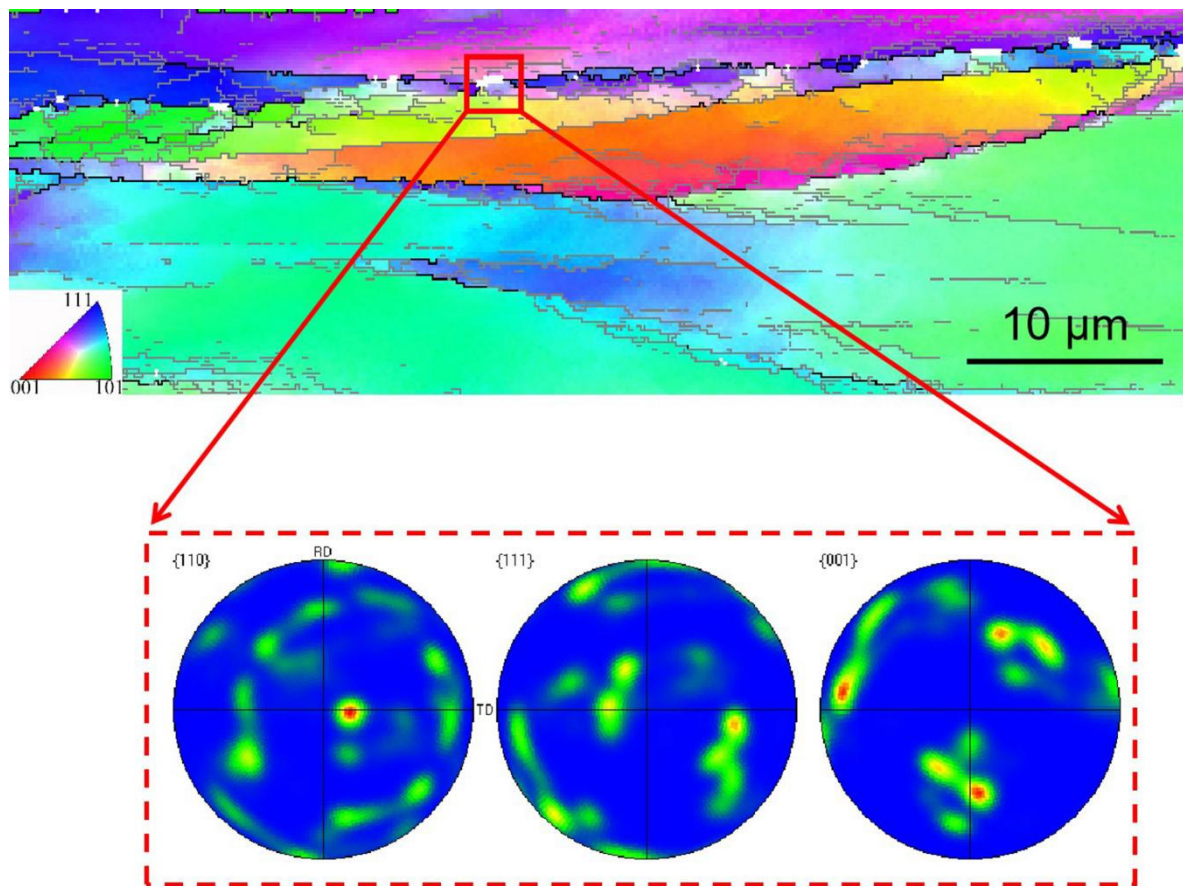


**Figure 9.** Pole figures (PFs) of a given local zone obtained from EBSD imaging at a true strain of 0.8 in the Ti-B12 alloy.

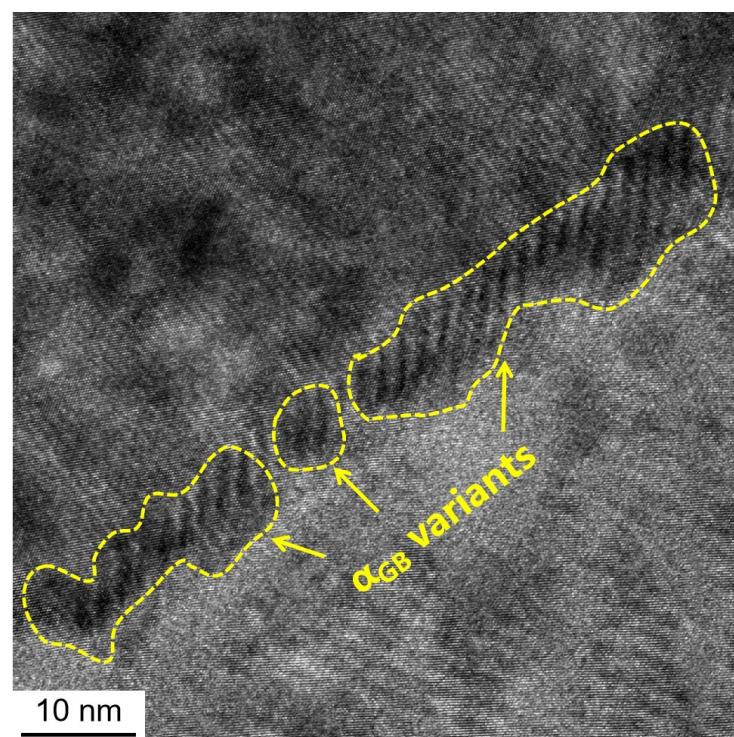


**Figure 10.** HRTEM image of hot-compressed microstructure at a true strain of 1.2 in the Ti-B12 alloy.

#### 4. Conclusions

The precipitation behavior of precipitated  $\alpha$  phase in Ti-B12 alloy was systematically investigated using SEM, TEM (HRTEM) and EBSD. The principal conclusions are as follows:

1. The volume fraction of  $\alpha$  phases precipitated within the parent  $\beta$  phase gradually increases with an increase in true strain. A large proportion of  $\alpha$  phases is prone to be precipitated at HAGBs and LAGBs during isothermal deformation. On the contrary, only a small amount of spherical  $\alpha$  phases is precipitated within the  $\beta$  grain.
2. The size of the precipitated  $\alpha$  phase during isothermal compression is much finer than that of  $\alpha$  precipitate during the same solution-plus-aging treatment. Some finer lath-shaped  $\alpha$  phases are generated after hot-compressed deformation. Meanwhile, some precipitated  $\alpha$  phases are non-uniformly distributed within the  $\beta$  grain.
3. The crystallographic orientation relationships for most of spherical  $\alpha$  precipitates formed at LAGBs and within the  $\beta$  grains are similar. On the contrary, the crystallographic orientation relationships for  $\alpha$  precipitates at grain boundaries are significantly different.

**Author Contributions:** Conceptualization: J.C.; methodology: J.C. and J.G.; software: J.C. and X.Z.; formal analysis: S.Y., J.Z. and Z.D.; data curation: J.C. and F.D.; writing—original draft preparation: J.C.; writing—review and editing: J.C. and J.G.; writing—manuscript finalization: J.C. and J.L.; supervision: J.C.; project administration: J.C. and S.Y.; funding acquisition: J.C. and S.Y. All authors have read and agreed to the published version of this manuscript.

**Funding:** This work was financially supported by the Key Research and Development Program of Shaanxi (Grant No. 2020GY-251); the National Natural Science Foundation of China (Grant No. 51901193, 51861029, 51801162 and 32071327); and the Science and Technology Project of Xi'an (Grant No. 2020KJRC0141).

**Institutional Review Board Statement:** Not applicable.

**Informed Consent Statement:** Not applicable.

**Data Availability Statement:** The raw data supporting the conclusions of this article will be made available by the authors without undue reservation.

**Conflicts of Interest:** The authors declare no conflict of interest, financial or otherwise.

#### References

1. Kolli, R.P.; Devaraj, A. A Review of Metastable Beta Titanium Alloys. *Metals* **2018**, *8*, 506. [[CrossRef](#)]
2. Raza, D.; Kumar, G.; Uzair, M.; Singh, M.K.; Sultan, D.; Kumar, R. Development and heat treatment of  $\beta$ -phase titanium alloy for orthopedic application. *Mater. Today Proc.* **2022**, *50*, 649–654. [[CrossRef](#)]
3. Hua, K.; Wan, Q.; Kou, H.; Zhang, F.; Zhang, Y.; Li, J. The interplay relationship between phase transformation and deformation behavior during hot compression in a metastable  $\beta$  titanium alloy. *Mater. Des.* **2021**, *197*, 109275. [[CrossRef](#)]
4. Pushp, P.; Dasharath, S.; Arati, C. Classification and applications of titanium and its alloys. *Mater. Today Proc.* **2022**, *54*, 537–542. [[CrossRef](#)]
5. Williams, J.C.; Boyer, R.R. Opportunities and issues in the application of titanium alloys for aerospace components. *Metals* **2020**, *10*, 705. [[CrossRef](#)]
6. Tiyyagura, H.R.; Kumari, S.; Mohan, M.K.; Pant, B.; Rao, M.N. Degradation behavior of metastable  $\beta$  Ti-15-3 alloy for fastener applications. *J. Alloys Compd.* **2019**, *775*, 518–523. [[CrossRef](#)]
7. Zhang, Y.; Xiang, S.; Tan, Y.B.; Ji, X.M. Study on  $\omega$ -assisted  $\alpha$  nucleation behavior of metastable  $\beta$ -Ti alloys from phase transformation mechanism. *J. Alloys Compd.* **2022**, *890*, 161686. [[CrossRef](#)]
8. Hua, K.; Zhang, Y.; Tong, Y.; Zhang, F.; Kou, H.; Li, X.; Wang, H.; Li, J. Enhanced mechanical properties of a metastable  $\beta$  titanium alloy via optimized thermomechanical processing. *Mater. Sci. Eng. A* **2022**, *840*, 142997. [[CrossRef](#)]
9. Song, B.; Xiao, W.; Fu, Y.; Ma, C.; Zhou, L. Role of nanosized intermediate phases on  $\alpha$  precipitation in a high-strength near  $\beta$  titanium alloy. *Mater. Lett.* **2020**, *275*, 128147. [[CrossRef](#)]
10. Xiao, W.; Dargusch, M.S.; Kent, D.; Zhao, X.; Ma, C. Activation of homogeneous precursors for formation of uniform and refined  $\alpha$  precipitates in a high-strength  $\beta$ -Ti alloy. *Materialia* **2020**, *9*, 100557. [[CrossRef](#)]
11. Du, Z.; Guo, H.; Liu, J.; Cheng, J.; Zhao, X.; Wang, X.; Liu, F.; Cui, X. Microstructure evolution during aging heat treatment and its effects on tensile properties and dynamic Young's modulus of a biomedical  $\beta$  titanium alloy. *Mater. Sci. Eng. A* **2020**, *791*, 139677. [[CrossRef](#)]

12. Wu, C.; Zhan, M. Microstructural evolution, mechanical properties and fracture toughness of near  $\beta$  titanium alloy during different solution plus aging heat treatments. *J. Alloys Compd.* **2019**, *805*, 1144–1160. [[CrossRef](#)]
13. Liu, Q.; Qiu, C. Variant selection of  $\alpha$  precipitation in a beta titanium alloy during selective laser melting and its influence on mechanical properties. *Mater. Sci. Eng. A* **2020**, *784*, 139336. [[CrossRef](#)]
14. Dong, R.; Kou, H.; Zhao, Y.; Zhang, X.; Yang, L.; Hou, H. Morphology characteristics of  $\alpha$  precipitates related to the crystal defects and the strain accommodation of variant selection in a metastable  $\beta$  titanium alloy. *J. Mater. Sci. Technol.* **2021**, *95*, 1–9. [[CrossRef](#)]
15. Zhao, Q.; Yang, F.; Torrens, R.; Bolzoni, L. Allotropic phase transformation and high-temperature tensile deformation behaviour of powder metallurgy Ti-5553 alloy. *Int. J. Refract. Met. Hard Mater.* **2020**, *90*, 105235. [[CrossRef](#)]
16. Hu, Z.; Zhou, X.; Nie, X.-A.; Zhao, S.; Liu, H.; Yi, D.; Zhang, X. Finer subgrain microstructure induced by multi-pass compression in  $\alpha + \beta$  phase region in a near- $\beta$  Ti-5Al-5Mo-5V-1Cr-1Fe alloy. *J. Alloys Compd.* **2019**, *788*, 136–147. [[CrossRef](#)]
17. Lin, Y.C.; Pang, G.-D.; Jiang, Y.-Q.; Liu, X.-G.; Zhang, X.-Y.; Chen, C.; Zhou, K.-C. Hot compressive deformation behavior and microstructure evolution of a Ti-55511 alloy with basket-weave microstructures. *Vacuum* **2019**, *169*, 108878. [[CrossRef](#)]
18. Qin, D.; Guo, D.; Zheng, L.; Li, Y. Dynamic recrystallization of Ti-5553 alloy during sub-transus thermomechanical processing: Mechanisms and its role in formation of a bi-modal structure. *J. Alloys Compd.* **2018**, *769*, 725–731. [[CrossRef](#)]
19. Qian, B.; Zhang, J.; Fu, Y.; Sun, F.; Wu, Y.; Cheng, J.; Vermaut, P.; Prima, F. In-situ microstructural investigations of the TRIP-to-TWIP evolution in Ti-Mo-Zr alloys as a function of Zr concentration. *J. Mater. Sci. Technol.* **2021**, *65*, 228–237. [[CrossRef](#)]
20. Wu, C.; Zhou, Y.J.; Liu, B. Experimental and simulated investigation of the deformation behavior and microstructural evolution of Ti6554 titanium alloy during an electropulsing-assisted microtension process. *Mater. Sci. Eng. A* **2022**, *838*, 142745. [[CrossRef](#)]
21. Hua, K.; Wan, Q.; Zhang, Y.; Kou, H.; Zhang, F.; Li, J. Crystallography and microstructure of the deformation bands formed in a metastable  $\beta$  titanium alloy during isothermal compression. *Mater. Charact.* **2021**, *176*, 111119. [[CrossRef](#)]
22. Zhou, L.; Sun, J.; Zhang, R.; Chen, J.; He, J.; Yuan, T. A new insight into the  $\alpha$  phase precipitation in  $\beta$  titanium alloy. *Vacuum* **2021**, *189*, 110272. [[CrossRef](#)]
23. Pang, G.-D.; Lin, Y.C.; Jiang, Y.-Q.; Zhang, X.-Y.; Liu, X.-G.; Xiao, Y.-W.; Zhou, K.-C. Precipitation behaviors and orientation evolution mechanisms of  $\alpha$  phases in Ti-55511 titanium alloy during heat treatment and subsequent hot deformation. *Mater. Charact.* **2020**, *167*, 110471. [[CrossRef](#)]
24. Coakley, J.; Vorontsov, V.A.; Jones, N.G.; Radecka, A.; Bagot, P.A.J.; Littrell, K.C.; Heenan, R.K.; Hu, F.; Magyar, A.P.; Bell, D.C.; et al. Precipitation processes in the beta-titanium alloy Ti-5Al-5Mo-5V-3Cr. *J. Alloys Compd.* **2015**, *646*, 946–953. [[CrossRef](#)]
25. Gupta, A.; Khatirkar, R.K.; Kumar, A.; Thool, K.; Bibhanshu, N.; Suwas, S. Microstructure and texture development in Ti-15V-3Cr-3Sn-3Al alloy—Possible role of strain path. *Mater. Charact.* **2019**, *156*, 109884. [[CrossRef](#)]
26. Zhang, R.; Ma, Y.; Qi, M.; Huang, S.; Youssef, S.S.; Xi, G.; Qiu, J.; Lei, J.; Yang, R.; Wang, P. The effect of precursory  $\alpha$  and  $\omega$  phase on microstructure evolution and tensile properties of metastable  $\beta$  titanium alloy. *J. Mater. Res. Technol.* **2022**, *16*, 912–921. [[CrossRef](#)]
27. Zharebtsov, S.; Murzinova, M.; Salishchev, G.; Semiatin, S. Spheroidization of the lamellar microstructure in Ti-6Al-4V alloy during warm deformation and annealing. *Acta Mater.* **2011**, *59*, 4138–4150. [[CrossRef](#)]
28. Chen, W.; Yu, G.; Li, K.; Wang, Y.; Zhang, J.; Sun, J. Plastic instability in Ti-6Cr-5Mo-5V-4Al metastable  $\beta$ -Ti alloy containing the  $\beta$ -spinodal decomposition structures. *Mater. Sci. Eng. A* **2021**, *811*, 141052. [[CrossRef](#)]
29. Chen, W.; Yang, S.; Lin, Y.; Chen, C.; Zhang, X.; Zhou, K. Multi-scale characterization of deformation features and precipitation behavior in a near  $\beta$ -Ti alloy. *Mater. Charact.* **2020**, *169*, 110637. [[CrossRef](#)]
30. Cheng, J.; Li, J.; Yu, S.; Du, Z.; Zhang, X.; Zhang, W.; Gai, J.; Wang, H.; Song, H.; Yu, Z. Influence of Isothermal  $\omega$  Transitional Phase-Assisted Phase Transition From  $\beta$  to  $\alpha$  on Room-Temperature Mechanical Performance of a Meta-Stable  $\beta$  Titanium Alloy Ti-10Mo-6Zr-4Sn-3Nb (Ti-B12) for Medical Application. *Front. Bioeng. Biotechnol.* **2021**, 1518. [[CrossRef](#)]
31. Dai, S.; Wang, Y.; Chen, F. Effects of annealing on the microstructures and mechanical properties of biomedical cold-rolled Ti-Nb-Zr-Mo-Sn alloy. *Mater. Charact.* **2015**, *104*, 16–22. [[CrossRef](#)]
32. Alabort, E.; Tang, Y.T.; Barba, D.; Reed, R.C. Alloys-by-design: A low-modulus titanium alloy for additively manufactured biomedical implants. *Acta Mater.* **2022**, *229*, 117749. [[CrossRef](#)]
33. Zhang, X.; Kou, H.; Li, J.; Zhang, F.; Zhou, L. Evolution of the secondary  $\alpha$  phase morphologies during isothermal heat treatment in Ti-7333 alloy. *J. Alloys Compd.* **2013**, *577*, 516–522. [[CrossRef](#)]
34. Dong, R.; Li, J.; Fan, J.; Kou, H.; Tang, B. Precipitation of  $\alpha$  phase and its morphological evolution during continuous heating in a near  $\beta$  titanium alloy Ti-7333. *Mater. Charact.* **2017**, *132*, 199–204. [[CrossRef](#)]
35. Fan, J.; Kou, H.; Lai, M.; Tang, B.; Chang, H.; Li, J. Hot deformation mechanism and microstructure evolution of a new near  $\beta$  titanium alloy. *Mater. Sci. Eng. A* **2013**, *584*, 121–132. [[CrossRef](#)]
36. Ding, R.; Gong, J.; Wilkinson, A.J.; Jones, I.P.  $\langle c + a \rangle$  Dislocations in deformed Ti-6Al-4V micro-cantilevers. *Acta Mater.* **2014**, *76*, 127–134. [[CrossRef](#)]
37. Elmer, J.W.; Palmer, T.A.; Babu, S.S.; Specht, E.D. Low temperature relaxation of residual stress in Ti-6Al-4V. *Scr. Mater.* **2005**, *52*, 1051–1056. [[CrossRef](#)]
38. Ivanov, A.; Orlov, A.; Golubovskii, E. The influence of thermomechanical processing on the structure and mechanical properties of rods made of high-strength titanium alloys of different classes. *Mater. Today Proc.* **2019**, *19*, 2163–2166. [[CrossRef](#)]
39. Mironov, S.; Murzinova, M.; Zharebtsov, S.; Salishchev, G.A.; Semiatin, S.L. Microstructure evolution during warm working of Ti-6Al-4V with a colony- $\alpha$  microstructure. *Acta Mater.* **2009**, *57*, 2470–2481. [[CrossRef](#)]

40. He, L.; Manshadi, A.D.; Dippenaar, R. The evolution of microstructure of Ti-6Al-4V alloy during concurrent hot deformation and phase transformation. *Mater. Sci. Eng. A* **2012**, *549*, 163–167. [[CrossRef](#)]
41. Furuhashi, T.; Takagi, S.; Watanabe, H.; Maki, T. Crystallography of grain boundary  $\alpha$  precipitates in a  $\beta$  titanium alloy. *Metall. Mater. Trans. A* **1996**, *27*, 1635–1646. [[CrossRef](#)]
42. Fan, J.K.; Kou, H.C.; Lai, M.J.; Tang, B.; Chang, H.; Li, J.S. Characterization of hot deformation behavior of a new near beta titanium alloy: Ti-7333. *Mater. Des.* **2013**, *49*, 945–952. [[CrossRef](#)]
43. Li, X.; Deng, S.; Wang, S.; Song, H.; Zhang, S.; Wang, K.; Ouyang, D. Dynamic globularization mechanism during hot working of Ti-6.5 Al-3.5 Mo-1.5 Zr-0.3 Si alloy with lamellar microstructure. *Mater. Charact.* **2021**, *171*, 110749. [[CrossRef](#)]